國立交通大學
電子物理研究所
碩士論文

氮化銦磊晶層之光學特性研究

Optical properties of InN epilayers

研 究 生：張尚樺

指導教授：周武清 教授

中華民國九十五年七月

氮化銦磊晶層之光學特性研究

Optical properties of InN epilayers

研 究 生：張尚樺　　Student： Shang-Hua Chang

指導教授：周武清 教授　　Advisor： Prof. Wu-Ching Chou

國立交通大學

電子物理研究所

碩士論文

A Thesis Submitted to
The Institute of Electrophysics
College of Science
National Chiao Tung University
In Partial Fulfillment of the Requirements
For the Degree of Master
In Electrophysics
July 2006
Hsinchu, Taiwan, Republic of China

中華民國九十五年七月

氮化銦磊晶層之光學特性研究

研究生：張尚樺　　指導教授：周武清 教授

國立交通大學電子物理研究所

中文摘要

本論文中我們利用光激螢光光譜和時間解析光譜來研究氮化銦磊晶層之光學特性。從霍爾量測的結果知道，成長氮化銦時緩衝層的基板溫度不同及緩衝層材料的不同皆會影響氮化銦磊晶層內載子濃度的多寡。從光激螢光光譜及吸收光譜的觀察，我們發現載子濃度的增加會同時使發光能量及吸收位置藍移，這樣的現象是由 Burstein-Moss 飄移所造成，量測到的實驗數據也與理論模型所計算的結果相符。從光激螢光光譜波形非常不對稱的情況，我們推測這是由於深層授子、淺層授子及 Urbach tail 存在於氮化銦磊晶層所造成。

從溫度變化的光激螢光光譜數據可得到兩個活化能，分別對應於另一

個研究團隊所提出的深層授子束縛能（50~55 毫電子伏特）及淺層授子和 Urbach tail 的束縛能（5~10 毫電子伏特）。從時間解析的激發-探測實驗，可以觀察到在室溫時隨著載子濃度的增加，載子的生命週期會同時有縮短的趨勢，呈現的大約是一次方反比的關係，因此得知氮化銦的 Auger 結合是相對較微弱的。當樣品處於低溫時，由變化激發強度的光激螢光實驗得知，在低溫下載子複合是由發光結合所主導。另外我們利用時間解析光激螢光光譜去觀察不同發光波長之受侷限的載子生命週期，隨著偵測能量的降低可以看到載子生命週期明顯的增加，透過載子侷限理論模型得到侷限深度大約為 10 毫電子伏特，與前述之淺層授子和 Urbach tail 的束縛能（5~10 毫電子伏特）相近。隨著溫度增加，被侷限的載子可獲得熱能而跳脫侷限使得生命週期變短。到目前為止，還沒有文獻報導氮化銦中授子及 Urbach tail 在載子結合的動態扮演的角色。在本論文的研究中，我們觀察到淺層授子和 Urbach tail 對於發光機制及載子結合的影響。

Optical properties of InN epilayers

Student: Shang-Hua Chang Advisor: Dr. Wu-Ching Chou

Institute of Electrophysics

National Chiao Tung University

Abstract

In this thesis, photoluminescence (PL) spectroscopy and time-resolved spectroscopy were used to investigate the optical properties of InN epilayers. From the Hall measurements, the carrier density of InN epilayers is strongly dependent on the substrate temperature and the material of buffer layer. Blue shifts of absorption edge and PL peak energy are due to the strong Burstein-Moss shift which results from the increasing carrier concentration. Our experimental data are consistent with the theoretical calculation. Typical PL spectra of highly asymmetric line-shape were attributed to the existence of Urbach tail and the shallow and deep acceptor states.

Two activation energies were obtained from integrated PL intensity versus inverse temperature plot. The small one is around 5~10 meV and the larger one is about 50~55 meV. These activation energies correspond to the binding energy of the shallow acceptors including the Urbach tail and the deep acceptors, respectively.

Pump-probe technique was used to study the carrier recombination dynamics at

room temperature. The room temperature carrier lifetime is inversely proportional to the carrier concentration. It reveals that the Auger recombination process does not contribute significantly. At low temperature, the power dependent PL study shows that the radiative recombination process dominates. The carrier lifetime at different emission energy was investigated by time resolved PL. The effect of exciton localization on the carrier recombination was observed. The depth of localization obtained by the theoretical fitting of localization model is about 10meV. Localization depth is very close to the binding energy of shallow acceptors and Urbach tail mentioned above. As the temperature was increased, the localized carriers may escape due to thermal excitation. As a result, the carrier life-time decreases abruptly with the increasing temperature. In this thesis, the influence of acceptors and Urbach tail in the recombination dynamics is shown to be crucial.

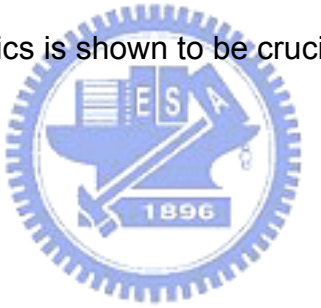

Acknowledgement

終於，在交大兩年的碩士班生活就要結束了。其實這兩年自己做了很多事，也學到了很多，當然這本論文的完成是這兩年中花最多心力的，過程中壓力很大但終究是克服了。畢業之後即將去當兵，我的學生生涯也要暫時地畫下句點，所以要特別的感謝在這些年當中教導、幫助及支持我的大家。

這本論文能夠完成，最由衷感謝的是指導教授周武清老師，在實驗的過程中提供許多資源及教導讓實驗可以順利的進行，在我最挫折而沒有方向的時候能夠給我良好的建議及希望還有在最後撰寫論文的這個階段仔細的和我一起討論跟修改，這些幫助對我來說都是相當重要的；也感謝這兩年來李明知老師、陳衛國老師及張文豪老師的教導，總是能提出許多一針見血的問題，雖然一開始不是那麼習慣而覺得很有壓力，但是在自己漸漸的成長之後發現這些都是非常重要的意見。而在實驗的過程中，阿邦學長一路的帶領跟陪伴也是這一年多來重要的支柱，如果沒有學長的協助我一定會遇到更多的挫折；也非常感謝古慶順、柯文政、李寧、京玉、文哲、謝博、祝壽、郭博、繼祖、彥丞、怡仁、狗哥及瑞泰這些學長們在實驗概念的教導和各方面的幫助。另外，還要特別感謝沈志霖老師、羅志偉老師及羅明華同學，如果沒有你們在實驗上的協助這篇論文是沒有辦法完成的。謝謝維偲、啟仁、泰鑫、羅士傑和戴士凱你們，雖然我個性比較孤僻一點點而和大家的互動比較少，但其實我很喜歡你們，也謝謝你們都能熱情的包容我。

另外，我還想謝謝鄭嘉良老師、賈至達老師、張煥正老師、蔡東昇學長及彭文平學長，你們過去的教導及帶領都是我成長過程中很重要的關鍵，也讓我有足夠的能力來面對這兩年碩士班的挑戰。

最後，當然最需要感謝的是我最親愛的家人、孟萱以及好友們，有你們在背後的支持都是我最大的精神力量來源，你們的陪伴是我能往前走的動力，謝謝你們大家。

Index

Chapter 1 Introduction

Recently, indium nitride (InN) has received much attention due to the discovery of its narrow direct band gap around 0.6~0.8 eV [1-5], in sharp contrast to previously reported band gap energy from 1.8~2.2 eV [6]. Therefore, the band gap of (Al, Ga, In)N system is now known to span from the ultraviolet of AlGaN to near infrared (IR) of InN, thus enabling the entire optical window to be included by a single material system [7]. This suggests that light emitting diode (LED) and laser diode (LD) operating in the wavelength range from infrared to ultraviolet can be fabricated by nitride compounds. In addition, InN is also a potentially important semiconductor material for the solar cell application [8]. However, the growth of high quality films has been difficult and with highly unintentional doping. Nevertheless, recent progress in the growth techniques made it possible to grow n-InN films with improved characteristics. There are already available samples with relatively lower concentration (~10^{17} cm^{-3}) and high mobility (~2100 cm^2/Vs) [9,10].

Photoluminescence (PL) experiments are widely used to investigate the nature of the recombination processes. Contrast to typical PL spectra that reveal one broad band with highly asymmetric lineshape, the well resolved structure consisting of three peaks was observed recently in the PL spectra of the high quality samples [11]. Klochikhin et al. explained the structure with a model calculation. They attributed one of the two low-energy features of the spectra to the recombination of degenerate electrons with the holes trapped by deep acceptors with a binding energy of E_{da}=0.050–0.055 eV, and the LO-phonon replica of this band. The higher-energy PL peak is considered as a complex band formed by two mechanisms. The first one is related to the transitions of electrons to the states of shallow acceptors with a binding

energy of E_{sh}=0.005–0.010 eV and/or to the states of the Urbach tail populated by photoholes. The second mechanism contributing to this band is the band-to-band recombination of free holes and electrons. These experimental data and model calculation results provide us a deeper understanding of physical properties of this material.

Even with the recent fast developments on the measurement and calculation of the physical and optical properties of InN, the investigation of carrier dynamics in InN is still lack. There are only some information provided by Chen et al. and Ascazubi et al. [12-16]. Chen et al. discussed the carrier lifetime for InN epilayers with unintentional doping level from 10^{18} to 10^{19} cm^{-3}. They found that the radiative recombination dominates at low temperature, and a defect related nonradiative recombination dominates at room temperature. They also observed the radiative lifetime increases proportionally to $T^{3/2}$ for the best quality sample, which suggests the radiative band to band free carrier transition.

However, contrast to the PL study that indicate the existence of deep acceptor, shallow acceptor and Urbach tail states, the investigation of recombination dynamics related to those states unknown. Thus, in order to understand the role of acceptors and Urbach tail in recombination dynamics of InN epilayers, the focus of this thesis is to detect the carrier recombination processes at different emission energy. This gives us another aspect of view to realize the influence of acceptor and Urbach tail states. Besides, this work could improve the understanding of the carrier recombination dynamics in InN.

Chapter 2 Theoretical Background

Optical characterization techniques are the most commonly used for measurement in the semiconductor industry. Optical measurements are attractive because they are almost always non-contacting with minimal sample preparation and nondestructive property. The instrumentation, for many optical techniques is commercially available and the measurements can have very high sensitivity. In this chapter, the photoluminescence mechanism and related knowledge [17-21] will be introduced.

For photoluminescence experiments, laser beam is absorbed by the semiconductor if the photon energy is larger than the semiconductor band gap. In the meantime, electrons and holes can be generated. The electrons and holes may be scattered and then redistribute near their respective conduction band minimum and valence band maximum, through the process of carrier-phonon interaction. Some electrons could be attracted by holes through Coulomb interaction to form excitons. Excitons could be further trapped by acceptors or donors. Free Excitons or trapped excitons could recombine radiatively and emit photons. Electrons/holes could also radiatively recombine with acceptors/donors. In some semiconductors, non-radiative transitions, which involves electrons and holes recombine with defects, could dominate. The emission efficiency is affected by the competition between radiative recombination and non-radiative recombination. In this chapter, radiative and non-radiative recombinations are discussed in detail as follows:

(A) Radiative Transition

Radiative recombination process includes (1) band to band transition, (2) excitonic recombination, and (3) defect (donor and/or acceptor) related transitions.

(I) Band to Band Recombination

Band to band transition involving free electrons in the conduction band minimum and holes in the valence band maximum usually occurs in direct-gap materials with the momentum conservation. The electron-hole pairs (e-h) will recombine radiatively. The recombination rate is almost proportion to the product of electron and hole concentrations, as shown in Fig. 2-1. But in the indirect band gap semiconductors, the transition must be assisted by an additional particle – “phonon” (in order to satisfy the momentum conservation rule). Thus, the radiative probability will be reduced, and the emission efficiency is much lower than the direct band gap semiconductors.

(II) Excitonic Recombination

Electron and hole can attract each other by the Coulomb interaction to form a hydrogen-like free exciton (FE) state. Its energy is slightly less than the band-gap energy required to create a separated electron-hole pair. An exciton can move through the crystal, but because it is a bound electron-hole pair, both electron and hole move together and neither photoconductivity nor current results. Free exciton recombination dominates when the material is sufficiently pure.

In another case, when a free hole can combine with a neutral donor to form a positively charged excitonic ion or bound exciton (BE). The electron bound to the donor travels in a wide orbit about the donor. Similarly electrons combining with neutral acceptors also form bound excitons. Bound exciton recombination dominates over free exciton recombination for less pure material. In these excitonic recombination processes, the photon energy is also less than the band-gap energy which similar to free exciton (FE). And in the direct band gap materials, this

phenomenon can explain by the Eq. 2-1:

$$h\nu = E_g - E_x \qquad \text{Eq. 2-1}$$

where E_x is the excitonic binding energy. Therefore, in indirect band-gap semiconductors, momentum conservation requires the emission of a phonon, giving

$$h\nu = E_g - E_x - E_p \qquad \text{Eq. 2-2}$$

where E_p is the phonon energy.

(III) Donor Acceptor Pair Recombination (DAP)

When both of the donor and acceptor concentrations of intentionally doped semiconductor or impure intrinsic semiconductor are not very low, the neutral donor electron and the acceptor hole could recombine, it can be expressed by:

$$D^0 + A^0 \rightarrow h\nu + D^+ + A^- \qquad \text{Eq. 2-3}$$

It can emit photon with an energy as described by the following formula:

$$E_{DAP} = h\nu = E_g - (E_D + E_A) + \frac{e^2}{\varepsilon \cdot R_{DA}} \qquad \text{Eq. 2-4}$$

Where, E_g is the energy gap of semiconductor, E_D and E_A is the respective binding energy for the electron to the donor and the hole to the acceptor. R_{DA} is the distance between the donor and the acceptor. If the R_{DA} increases, the transition probability will reduce, so does the PL intensity.

(B) Non-Radiative Transition

Electrons and holes can recombine nonradiatively. In fact, in many semiconductors the nonradiative transition is the dominant process. There are several recombination processes which do not result in external photon emission and thus reduce the emission efficiency. They are depicted as follows:

(I) The e-h pair is scattered by the phonon or carriers and loses its energy.

(II) The e-h pair recombines at defect, dislocation, grain boundary or surface, and

loses its excess energy, the so-called “cascade process”.

(III) In the Auger effect, the energy released by a recombining electron is immediately absorbed by another electron which then dissipates this energy by emitting phonons. Thus this three-body collision, involving two electrons and a hole, results in no net photon emission. Auger process increases its importance with the increasing carrier concentration.

All the non-radiation transitions will compete with radiation transitions, the stronger the non-radiation transition, the lower the PL intensity.

(C) Carrier Lifetime

Carrier lifetime is an useful information to understand the mechanism of recombination processes. Photoluminescence decay is one of optical measurements to obtain the carrier lifetime. Carriers can be generated by a short pulse of incident photons with energy $h\nu > E_g$. When the laser ceases, the excited carrier will exponentially decay, as the following equation 2-5:

$$N(t) = N_0 \exp(-t/\tau) \qquad \text{Eq. 2-5}$$

Where, $N(t)$ is the density of excess carrier, N_0 is the density of injected carriers, t is the delay time, and τ is the time constant. The light intensity $I(t)$ is given by the following equation:

For the light intensity I(t) we have

$$I(t) \sim -\frac{dN(t)}{dt} = \frac{N_0}{\tau} e^{-t/\tau} = I_0 e^{-t/\tau} \qquad \text{Eq. 2-6}$$

Because of the special properties of the exponential function, the light intensity decays with the same time constant τ as the carrier population decay.

We will consider a n-type semiconductor throughout this introduction. The recombination rate R depends nonlinearly on the departure of the carrier densities

from their equilibrium values. If we confine to linear, quadratic, and third-order terms, then R can be written as:

$$R=A(n-n_0)+B(pn-p_0n_0)+C_p(p^2n-p_0^2n_0)+C_n(pn^2-p_0n_0^2) \quad \text{Eq. 2-7}$$

Where, A is the Shockley-Read-Hall recombination coefficient, B is the radiative recombination coefficient, C_p is the Auger recombination coefficient for holes, C_n is the Auger recombination coefficient for electrons, $n=n_0+\Delta n$, $p=p_0+\Delta p$, n_0 and p_0 are the respective electron and hole equilibrium densities, and Δn and Δp the excess electron and hole densities. In the absent of trapping, $\Delta n=\Delta p$, allowing R to be simplified to

$$R\sim A\,\Delta n+B(n_0+\Delta n)\,\Delta n+C_p(p_0^2+2p_0\,\Delta n+\Delta n^2)\,\Delta n+C_n(n_0^2+2n_0\,\Delta n+\Delta n^2)\,\Delta n \quad \text{Eq. 2-8}$$

Here, some terms containing p_0 have been dropped because $n_0 >> p_0$ in a n-type material. The recombination lifetime is defined as

$$\tau_r=\frac{\Delta n}{R} \quad \text{Eq.2-9}$$

which gives

$$\tau_r=\frac{1}{A+B(n_0+\Delta n)+C_p(p_0^2+2p_0\,\Delta n+\Delta n^2)+C_n(n_0^2+2n_0\,\Delta n+\Delta n^2)} \quad \text{Eq. 2-10}$$

Three main recombination mechanisms determine the recombination lifetime: Shockley-Read-Hall or multiphonon recombination characterized by the lifetime τ_{SRH}, radiative recombination characterized by τ_{rad} and Auger recombination characterized by τ_{Auger} (details will be discussed later). The three recombination mechanisms are illustrated in Fig. 2-2. The recombination lifetime τ_r is determined by the three mechanisms according to the relationship

$$\frac{1}{\tau_r}=\frac{1}{\tau_{SRH}}+\frac{1}{\tau_{rad}}+\frac{1}{\tau_{Auger}} \quad \text{Eq. 2-11}$$

(I) Shockley-Read-Hall recombination

During SRH recombination, electron-hole pairs recombine through the

assistance of deep-level impurities, characterized by the impurity density N_T, energy level E_T in the band gap, and capture cross sections σ_n and σ_p for electrons and holes, respectively. The energy liberated during the recombination event is dissipated by lattice vibrations or phonons, illustrated in Fig. 2-2(a). The SRH lifetime is given by

$$\tau_{SRH} = \frac{\tau_p(n_0 + n_1 + \Delta n) + \tau_n(p_0 + p_1 + \Delta p)}{p_0 + n_0 + \Delta n} \qquad \text{Eq. 2-12}$$

where n_1, p_1, τ_n and τ_p are defined as

$$n_1 = n_i \exp\left[\frac{(E_T - E_i)}{KT}\right] \qquad \text{Eq. 2-13-1}$$

$$p_1 = n_i \exp\left[\frac{-(E_T - E_i)}{KT}\right] \qquad \text{Eq. 2-13-2}$$

$$\tau_p = \frac{1}{\sigma_p \nu_{th} N_T} \qquad \text{Eq. 2-13-3}$$

$$\tau_n = \frac{1}{\sigma_n \nu_{th} N_T} \qquad \text{Eq. 2-13-4}$$

and ν_{th} represent the carrier velocity. Equation τ_{SRH} can be simplified for low-level and high level injection. For low-level hole injection, the excess minority carrier density is low compared to the equilibrium majority carrier density, $\Delta n << n_0$. Similarly high-level injection holds when $\Delta n >> n_0$.

For the low level injection,

$$\tau_{SRH} \approx \tau_p \frac{n_1}{n_0} + \tau_n \frac{p_1}{n_0} \approx \tau_p = \frac{1}{\sigma_p \nu_{th} N_T} \qquad \text{Eq. 2-14}$$

While, for the high level injection,

$$\tau_{SRH} \approx \tau_p + \tau_n = \frac{1}{\sigma_p \nu_{th} N_T} + \frac{1}{\sigma_n \nu_{th} N_T} \qquad \text{Eq. 2-15}$$

(II) Radiative recombination

During radiative recombination electron-hole pairs recombine directly from band to band with the energy carried away by photons shown in Fig. 2-2(b). The radiative lifetime is

$$\tau_{rad} = \frac{1}{B(p_0 + n_0 + \Delta n)} \qquad \text{Eq. 2-16}$$

Where, B is the radiative recombination coefficient. The radiative lifetime is inversely proportional to the carrier density because in band-to-band processes both electrons and holes must be present simultaneously for a recombination event to take place.

For the low level injection,

$$\tau_{rad} \approx \frac{1}{B\, n_0} \qquad \text{Eq. 2-17}$$

For the high level injection,

$$\tau_{rad} \approx \frac{1}{B\, \Delta n} \qquad \text{Eq. 2-18}$$

(III) Auger recombination

During the Auger recombination, illustrated in Fig. 2-2(c), the recombination energy is absorbed by a third carrier. Because three carriers are involved in the recombination event, the Auger lifetime is inversely proportional to the square of the carrier density. For a n-type semiconductor, the Auger lifetime is given by

$$\tau_{Auger} = \frac{1}{C_p\,(p_0^2 + 2p_0\,\Delta n + \Delta n^2) + C_n\,(n_0^2 + 2n_0\,\Delta n + \Delta n^2)} \approx \frac{1}{C_n\,(n_0^2 + 2n_0\,\Delta n + \Delta n^2)} \qquad \text{Eq. 2-19}$$

Where, C_p is the Auger recombination coefficient for holes and C_n for electrons.

For the low level injection,

$$\tau_{Auger} \approx \frac{1}{C_n\, n_0^2} \qquad \text{Eq. 2-20}$$

For the high level injection,

$$\tau_{Auger} \approx \frac{1}{(C_p + C_n)\,\Delta n^2} \qquad \text{Eq. 2-21}$$

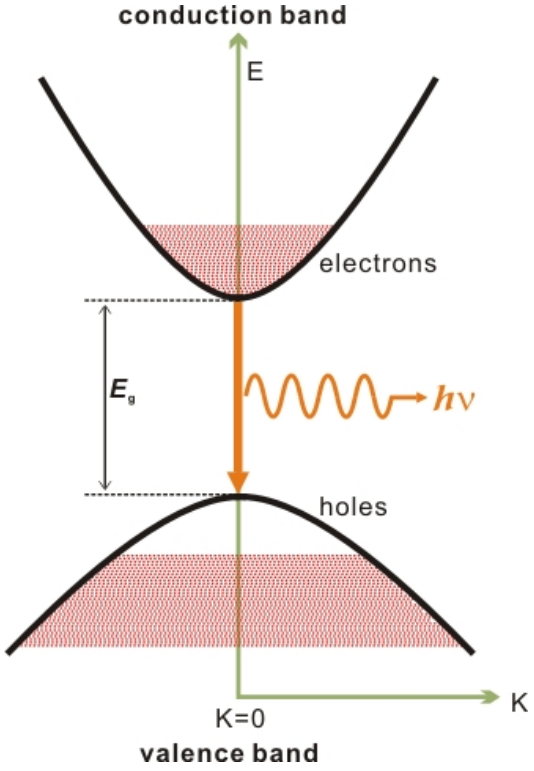

(a) Direct transition

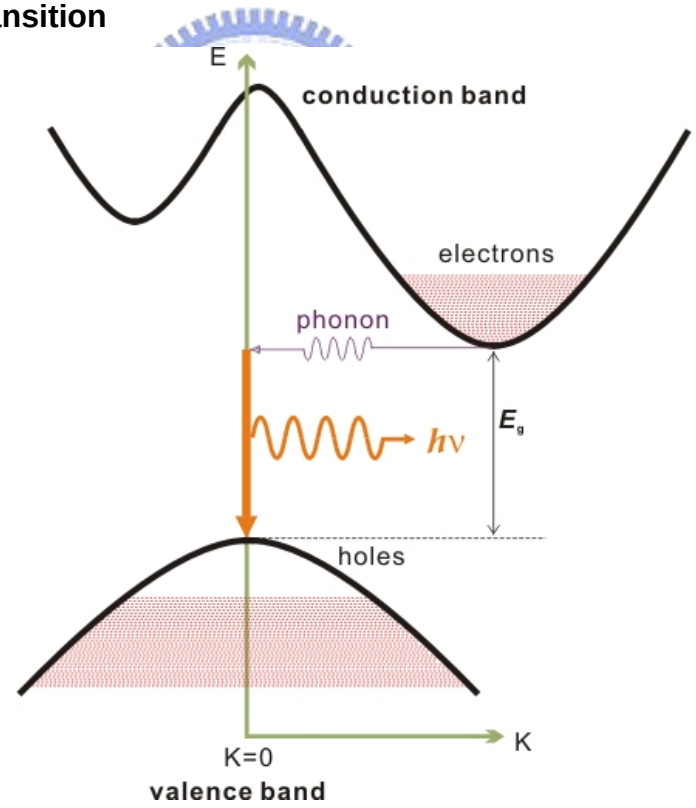

(b) Indirect transition

Fig. 2-1 Schematic representations for the (a) direct and (b) indirect transition.

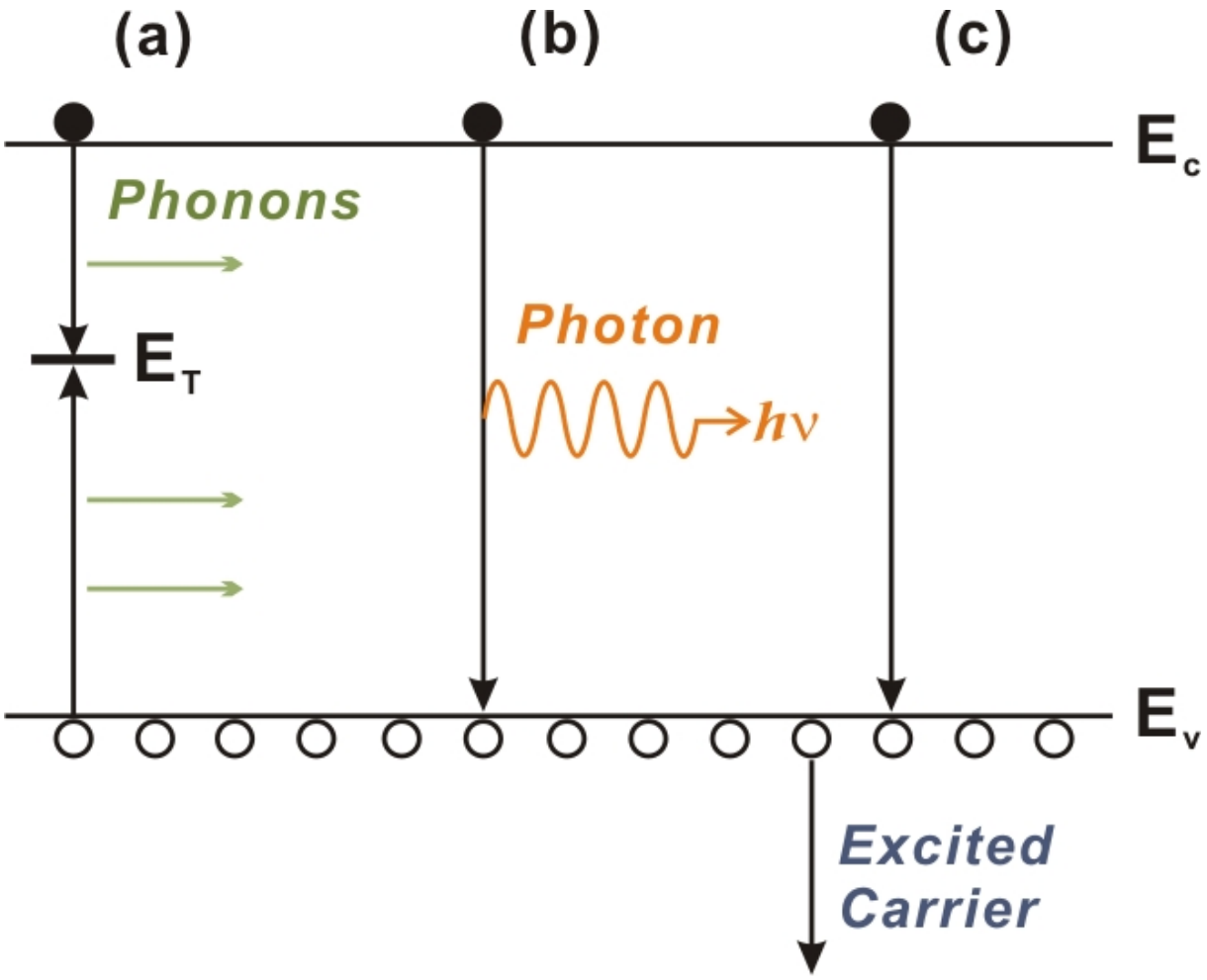

Fig. 2-2 Recombination mechanisms: (a) SRH, (b) radiative, (c) Auger.

Chapter 3 Experiment

In this chapter, experimental details of sample preparation of the InN epilayers, macro-photoluminescence (PL) spectroscopy and time resolved spectroscopy will be described.

3.1 Sample preparations

The samples were grown by MOVPE using trimethylgallium (TMGa), trimethylindium (TMIn) and NH_3 as source materials. The main InN epilayers were grown on GaN/sapphire (0001) with layer thickness of 500 nm. The quality of InN epilayers could be controlled by varying the substrate temperatures (T_S) from 600 to 650℃. The source flow rates for TMIn and NH_3 were 360 sccm and 15000 sccm, respectively. The Hall measurement of these InN epilayers shows a highly unintentional doping. Details of sample parameters are listed in Table 3.1. In order to decrease the carrier concentration of InN for better optical quality, the InN epilayer was grown on InGaN/GaN/sapphire (0001) with same layer thickness of 500 nm. A schematic diagram of the sample structure was shown in Fig. 3-1.

Table 3-1 Sample parameters.

Sample	Carrier concentration (cm^{-3})	T_s (^oC)	InN thickness	Structure
A	4.8×10^{18}	625	500 nm	InN/ InGaN/ GaN
B	6.4×10^{18}	650	500 nm	InN/ GaN
C	1.1×10^{19}	625	500 nm	InN/ GaN
D	1.3×10^{19}	600	500 nm	InN/ GaN

3.2 Macro Photoluminescence system and Time-resolved PL system

A schematic of set-up of Macro-PL system is shown in Fig. 3-2. The 488-nm line of an argon-ion laser (Coherent Innova 90) is used as the excitation light source. The excitation intensity was about 5W/cm^2, and the focused spot size is about 1mm^2. The laser beam was chopped and focused by a lens (f =10cm), the laser spot focused on the sample surface. Samples were mounted at sample holder that was made of copper. The emission lights were collected by a collecting lens (f =15cm) and the reflective light of laser was avoided. The collected light was focused by a lens (f =28cm) and passed through a long pass filter (1 micron) to cut off the laser signals. Then, the signal light entered a monochromator through the entrance slit. The PL detection system includes a grating 0.27-m monochromator (Spex 270M) equipped with an un-cooled InGaAs photodetector (cut-off wavelength at 2.05 μm). The detected signals were amplified by a standard lock-in amplifier, and input to the SpectrACQ2. All signals were analyzed by the SpetraMax software. Temperature dependent PL measurements were carried out using a closed cycle cryogenic system. The temperature was varied from 10 K to 300K by a Lakeshore 331 temperature controller.

The setup of time-resolved PL is shown in Fig. 3-3. PL decay measurements were made using pulsed diode lasers operating at wavelengths of 976 nm. The diode laser produces light pulse width of about 56 ps and a repetition rate of 40 MHz. The luminescence was directly collected onto a spectrometer and then detected by a high-speed photomultiplier tube (PMT), which was cooled down to -60^{o}C. PL decay signals were analyzed using the technique of time-correlated single-photon counting (TCSPC) by a PC plug-in time-correlated counting card. The overall temporal resolution of the apparatus is about 300 ps.

3.3 Femtosecond time-resolved spectroscopy

The principle of monitoring an ultrafast event by the pump-probe technique is illustrated in Fig. 3-4(a), where both pump and probe pulses are synchronized. For an event, n(t), to be measurable via the pump-probe technique, its lifetime must not exceed the separating time, 13 ns, between two pumping pulses. Since n(t) is triggered by a laser (pump) pulse train, n(t) shows its replica with a period of 13 ns. Assuming that the n(t) could be related to the index of reflection, the reflective (or transmissive) intensity of probe pulses from sample will vary with n(t) while the probe pulses temporally overlapped with n(t). However, this change due to n(t) is very small, typically between 10^{-5} ~ 10^{-7}, and is very difficult to be detected directly under the noisy background (including laser noise, electronic noise, mechanic vibration etc.) by photodiode. Hence, the phase-lock technique was usually used to provide a background-free signal.

The modulation was commonly applied to the pump pulse train to make sure that the signal merely came from the $\mathrm{n}(t)$ induced by pump pulses. Then, the probe pulse train was also modulated by the $\mathrm{n}(t)$ on the constant intensity of the probe pulse train, i.e. a AC signal $(\Delta I(t))$ is added to a DC signal $(I_0(t))$. This signal was detected by the photodiode and fed to the lock-in amplifier, which was phaselocked to the accusto-optic modulator. The lock-in amplifier merely extracted the AC signal $(\Delta I(t))$, of which frequency was exactly equal to the modulating frequency and in-phase with the modulator. Additionally, the DC component $(I_0(t))$ was detected by the multimeter. By varying the time delay (t) between pump and probe pulses, $\Delta I(t)$ would change as a function of time delay. Therefore, the temporal evolution of $\mathrm{n}(t)$ could be measured by assuming that the relation between $\mathrm{n}(t)$ and $\Delta I(t)$ is linear. Finally, the AC signal $(\Delta I(t))$ should be normalized by the DC component $(I(t))$ for the whole curve to

eliminate the zero-point drift due to the long-term fluctuations of the laser intensity. According to the relation

$$\frac{\Delta R}{R} = \frac{R_{pump\ \ open} - R_{pump\ \ closed}}{R_{pump\ \ closed}} = \frac{[(\frac{I_r}{I_i})_{pump\ \ open} - (\frac{I_r}{I_i})_{pump\ \ closed}]}{(\frac{I_r}{I_i})_{pump\ \ closed}} \qquad \text{Eq. 3-1}$$

$$= \frac{(I_r)_{pump\ \ open} - (I_r)_{pump\ \ closed}}{(I_r)_{pump\ \ closed}} = \frac{\Delta I}{I_0}$$

where $(I_i)_{\text{pump open}} = (I_i)_{\text{pump closed}}$ and $(I_r)_{\text{pump closed}} \equiv I_0$, one could obtain the relative changes in reflectivity $\Delta R/R$ (or transmissivity $\Delta T/T$) of the order of 10^{-6} by directly measuring the $\Delta I/I_0$. It is noted that $\Delta R/R$ is independent of the intensity of incident light (I_i), and therefore allows us to make a comparison between various measurements.

Fig. 3-4(b) depicts the experimental setup in this study. The femtosecond pulses from Ti:sapphire laser went through two prisms to pre-chirp the pulses. Two lenses were used to reduce the diameter of the laser beam which was enlarged by the prisms. The beamsplitter reflected 50 % of light in the pump channel, whereas the remnant was transmitted and served as the probe. Both pump and probe beams went through two acousto-optic modulators (AOM), respectively. But, only one in the pump beam was driven by the RF driver and modulated the pump beam at given frequency. After the delay stage, the halfwave (λ/2) plate, and the polarizer, the pump beam was focused on the surface of sample with 125 μm in diameter by the 200 mm lens. On the other hand, the probe beam only went through the λ/2 plate and polarizer after the AOM and was focused on the surface of samples with 84 μm in diameter by the 150 mm lens. The spatial overlap of pump and probe beams on the sample was monitored by a CCD camera. The reflection of the probe beam was received by the photodiode. The delay stage (delay time, t) was controlled by a computer to measure $(\Delta R/R(t))$.

The light source used in this study was a mirror-dispersion-controlled Ti:sapphire oscillator (Mode: C20) fabricated by Femto Lasers in Vienna. Here, we used a

Coherent Innova 90 Ar^+ laser as the pump source. The pump power was 4.6 W and the average output power of the mirror-dispersion-controlled Ti:sapphire oscillator was 700 mW with 20 fs in the pulsewidth, 800 nm in the center wavelength, and 75 MHz in the repetition rate.

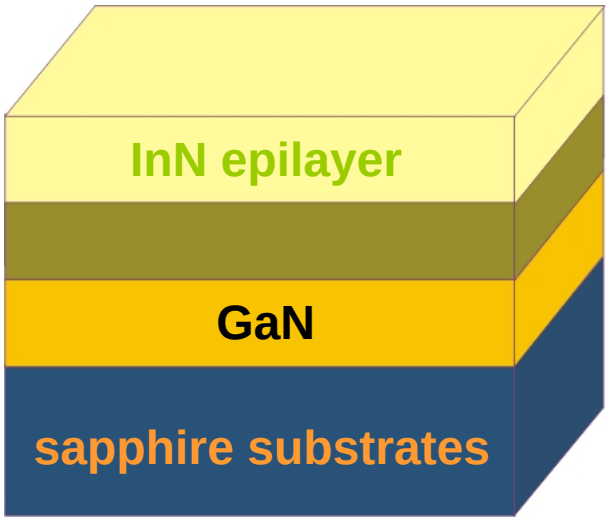

(a) Sample A (InN/InGaN/GaN)

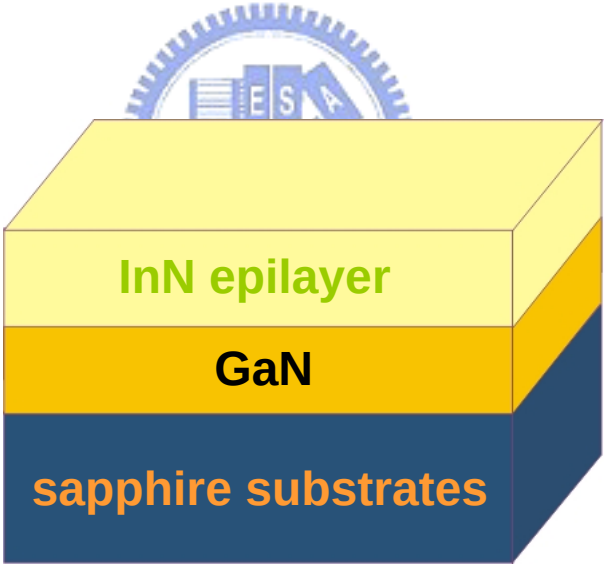

(b) Sample B, C and D (InN /GaN)

Fig. 3-1 A schematic diagram of sample structure (a) sample A, (b) sample B, C and D.

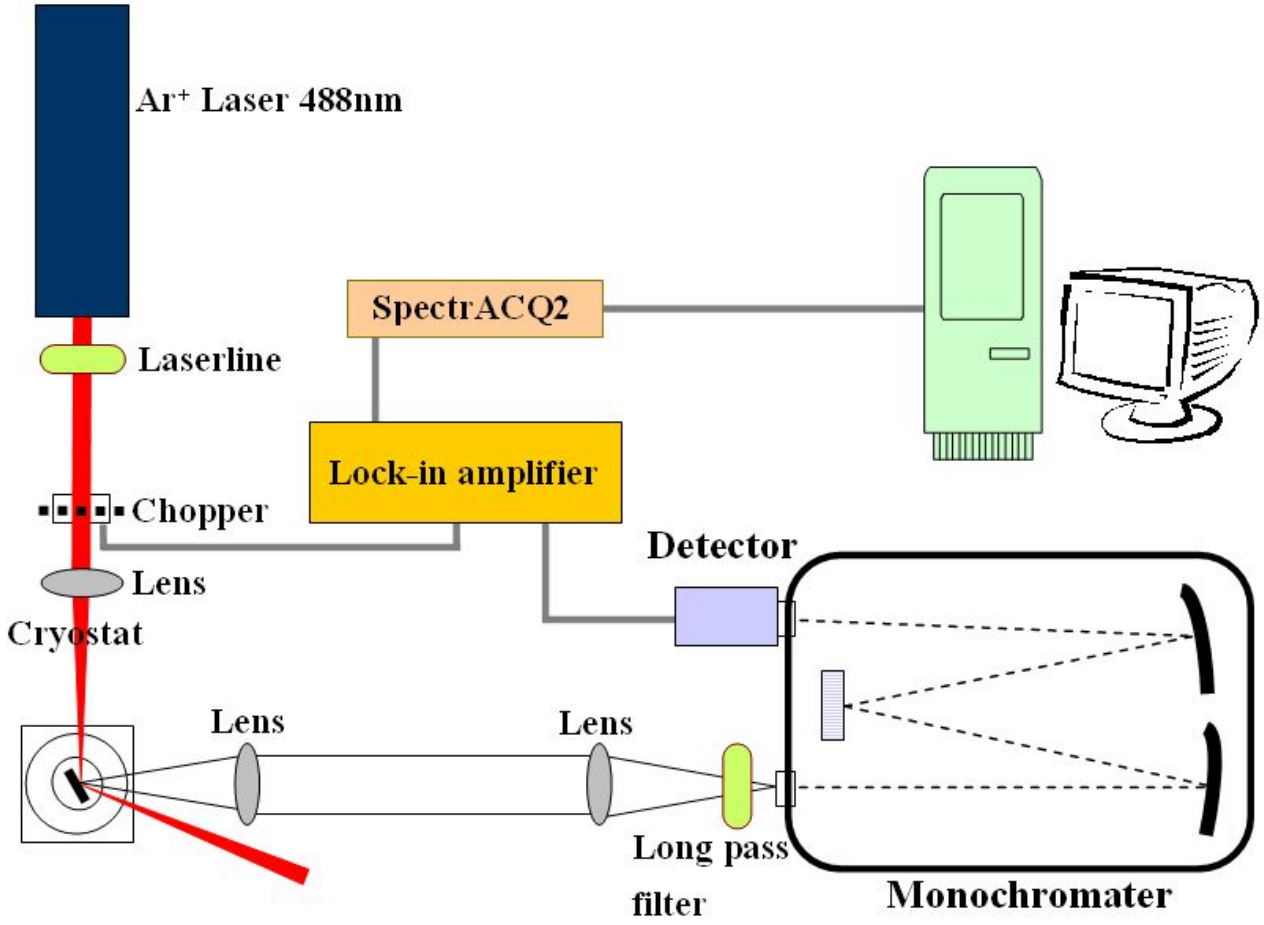

Fig. 3-2 Diagram of photoluminescence system.

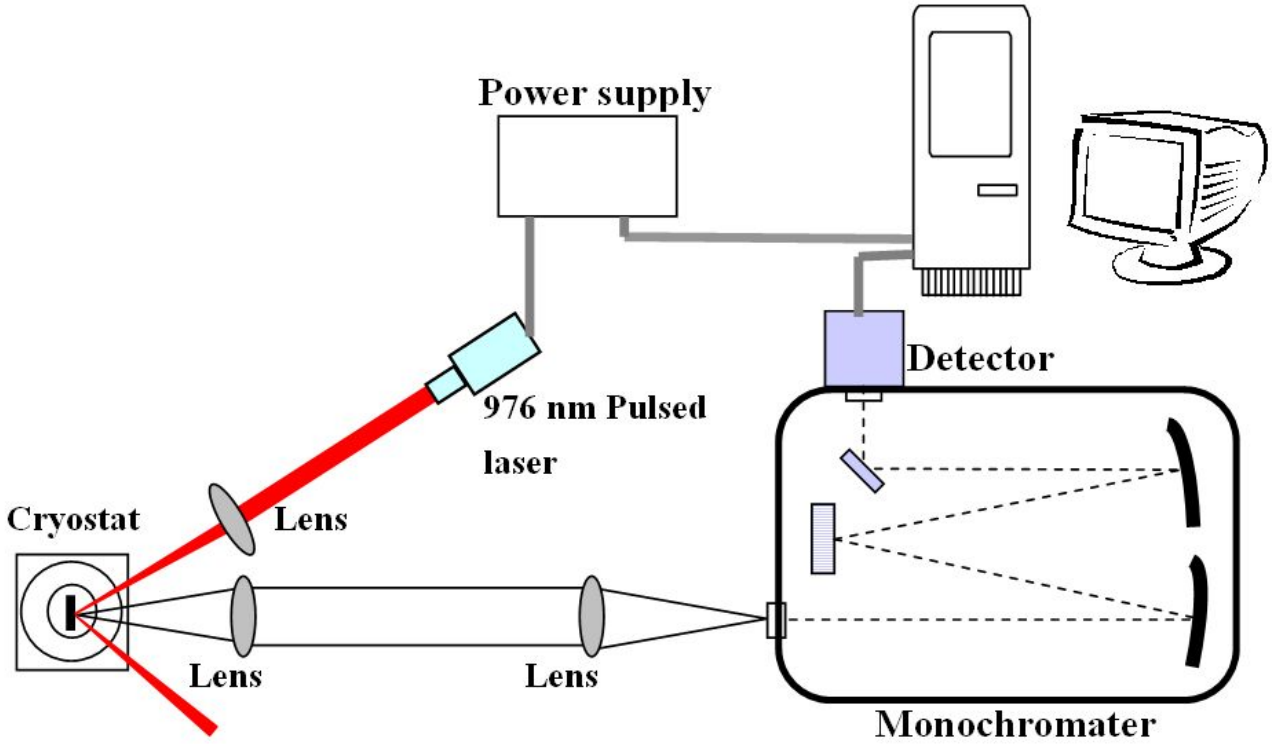

Fig. 3-3 Diagram of time-resolved photoluminescence (TRPL) system.

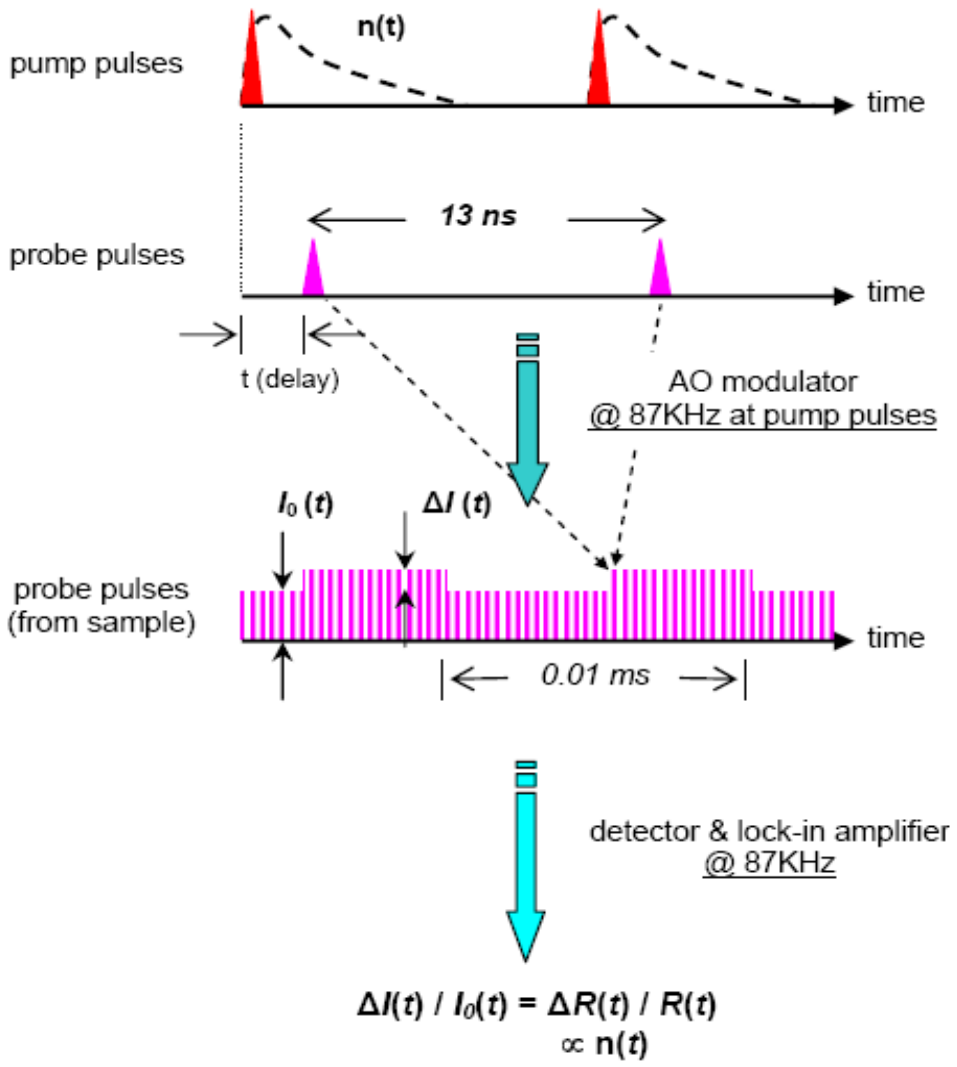

Fig. 3-4 Illustration for the pump-probe technique.

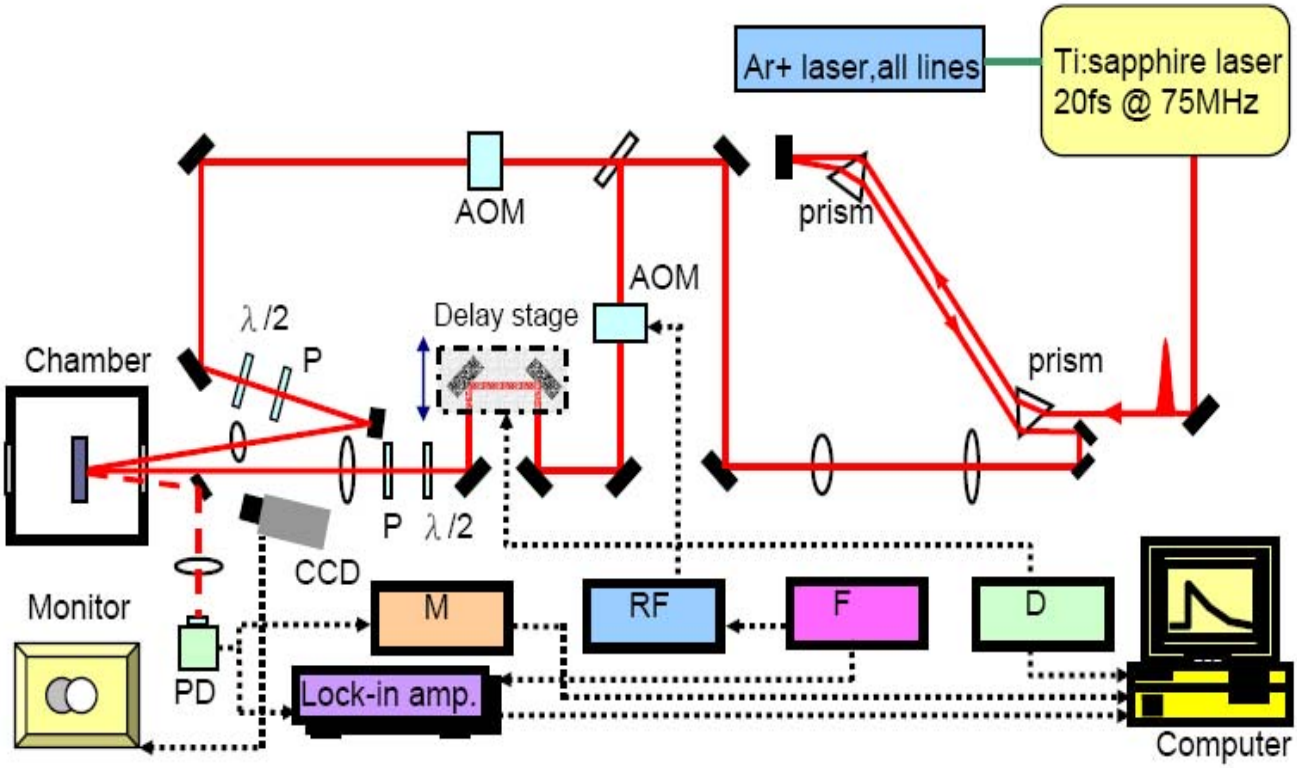

Fig. 3-5 The experimental setup for near-IR pump-probe spectroscopy.

The short writing AOM, P, CCD, PD, M, RF, F and D represent acousto-optic modulator, polarizer, CCD camera, photodiode, multimeter, RF driver, function generator and delay controller, respectively. The solid and dashed lines represent the laser beam path and the dotted lines stand for the electrical signal connection.

Chapter 4 Results and Discussion

In this chapter, the photoluminescence spectra and absorption spectra of InN epilayers were investigated in order to study the recombination mechanisms. Temperature-dependent PL spectra were analyzed to obtain the activation energy. Furthermore, time-resolved spectroscopy and power-dependent PL spectra were used to investigate the information about carrier recombination processes.

4.1 Emission and absorption properties of InN epilayers

Fig. 4-1 shows the typical PL spectra of the InN epilayer with high electron concentration at low temperature. The strong PL emission near 0.7 eV is consistent with the observations of other groups in recent years [1-5]. As the free-electron concentration increases, both the emission width and peak energy increase simultaneously. The peak energy and full width at half maximum (FWHM) are measured as 0.719 eV and 57 meV for sample A, 0.739 eV and 73 meV for sample B, 0.764 eV and 82 meV for sample C, and 0.784 eV and 90 meV for sample D at 15K. These emission energies are slightly higher than the reported band gap energy of 0.69 eV [11], indicating a bandfilling effect due to the presence of high electron concentration. As shown in this figure, the spectral shape of the emission band is highly asymmetric, and the phenomenon is reasonably explained by the existence of the deep acceptors, shallow acceptors, and Urbach tails [11]. The dashed lines in Fig. 4-1 are absorption spectra measured at 15K. The absorption edge and PL peak energy both blue shift as free-carrier concentration increases due to the strong Burstein-Moss effect. The absorption edges in these spectra are larger than the peak energies of PL spectra, because absorption occurs significantly above the Fermi-level at low temperature. Fig. 4-2(a) schematically shows the difference between the

absorption mechanism and PL mechanism. In order to understand the relationship between the absorption edge and the carrier concentration, our measurement results were compared with the theoretical calculation in Fig. 4-2(b). The solid line is the calculated band gap assuming a nonparabolic dispersion for the conduction band and including the band-renormalization effects [22]. The dotted-dashed line is the same calculation but without including the band-renormalization effects. The dotted line is the result of a calculation assuming a parabolic conduction band, and the solid circle are experimental data observed by J. Wu et al. The open squares are absorption edge at room temperature of our samples, they are consistent with the theoretical results that including conduction band nonparabolicity and band-renormalization effects.

In order to identify the mechanism of PL quenching, the temperature dependence of the integrated PL intensity of InN epilayers are shown in Fig. 4-3. All of the experimental data were fitted with the following model involving two activation mechanisms described by [23, 24]

$$I = I_0[1 + C_1 \exp(-E_{a1}/k_B T) + C_2 \exp(-E_{a2}/k_B T)]^{-1} \quad \text{Eq. 4-1}$$

where I is the integrated PL intensity, I_0 is the integrated PL intensity at 15 K, C_1 and C_2 are the fitting constants, E_{a1} and E_{a2} are the activation energies at two different temperature regions. E_{a1} of these samples are about 8 meV for the low temperature range, and are roughly the same with E_{sh}~5-10 meV that demonstrated as the binding energy of shallow acceptor and/or Urbach tail. E_{a2} of these samples are about 60 meV for the high temperature range, also are close to E_{da}~50-55 meV that indicated as the binding energy of the holes trapped by deep acceptors. The activation may be attributed to electrons or holes thermally detrapped from shallow and deep acceptor states into valance band [11].

Fig. 4-4 shows the integrated PL intensity on the logarithmic scale as a function

of the excitation power for sample A, B,C and D. The dependence is characterized by

$$I_{PL} = \beta I_{ex}^{m} \qquad \text{Eq. 4-2}$$

where $\boldsymbol{I_{PL}}$ is the integrated PL intensity, $\boldsymbol{I_{ex}}$ is the intensity of the excitation, β is a coefficient which depends on temperature and the exponent *m* can be used to characterize the emission mechanism [25, 26]. If the relation between $\boldsymbol{I_{PL}}$ and $\boldsymbol{I_{ex}}$ displays a linear dependence (*m*=1), indicating that most of the injected carriers recombine radiatively. However, if the exponent *m* becomes 2/3, indicating the ideal value for Auger process that carriers recombine nonradiatvely. In this figure, all dashed lines are linear dependence (*m*=1) and the symbols stars, circles, triangles and squares are experiment results of samples A, B, C and D, respectively. Thus, the power dependence measurements at low temperature (15K) reveal that the radiative recombination dominates in these InN samples.

4.2 Carrier dynamics of InN epilayers

In order to understand more about the carrier recombination dynamics, the time-resolved spectroscopy was used to measure the decay time of our InN samples. Fig. 4-5(a) shows the measured time resolved differential reflectance signals as a function of time delay. The excitation was a 800nm and femtosecound pulse laser. The pumping fluence was fixed at 120μJ/cm^2. The reflectivity decay are fitted by a single exponential exp(-t/ τ), to obtain the decay time τ for our measurements. Lifetime are fitted as 133ps for sample A, 65ps for sample B, 45ps for sample C and 27ps for sample D. The dependences of carrier lifetimes on the carrier concentrations are illustrated in Fig. 4-5(b), results from other groups were also included for comparison [14]. For samples investigated here, the carrier lifetime is found almost inversely proportional to the free carrier concentration. It is well known that the

recombination of the photogenerated carriers through three different processes: Shockley-Read-Hall or multiphonon recombination characterized by τ_{SRH}, radiative recombination characterized by τ_{rad} and Auger recombination characterized by τ_{Auger}. Thus, the carrier lifetime is described by [18]

$$\frac{1}{\tau} = \frac{1}{\tau_{SRH}} + \frac{1}{\tau_{rad}} + \frac{1}{\tau_{Auger}} = \frac{1}{\sigma v N_{defect}} + B_{rad}(n+n_0) + C_{Auger}(n+n_0)^2 \quad \text{Eq. 4-3}$$

This equation was mentioned in chapter 2 in more details. In this equation, σ is the carrier capture cross section, ν is the carrier velocity, N_{defect} represents the defect density, n is the photogenerated carrier density, n_o is the free-electron concentration, B_{rad} represents the radiative recombination coefficient and C_{Auger} represents the Auger recombination coefficient. From this equation, we realize that the carrier lifetime is inversely proportional to n_o and n_o^2 for radiative recombination and nonradiative Auger recombination respectively, and the defect related nonradiative SRH recombination rate is proportional to the defect density. Thus, the inverse proportionality between free electron concentration and carrier decay time, observed in Fig. 4-5(b), reveals that the Auger recombination does not contribute significantly to the carrier recombination. In addition, we calculate the Auger recombination coefficient by using the equation that derived by Ridley [27, 28],

$$w = \frac{2\pi^{1/2} e^4 m_e^* (kT)^{3/2} [(\frac{m_e^*}{m_0}) + (\frac{m_e^*}{m_h^*})]}{(\varepsilon_0 \varepsilon_r)^2 h^3 [1 + (\frac{m_e^*}{m_h^*})]^{1/2} E_g^{3/2}} \times \exp[-\frac{(1+\frac{m_e^*}{m_h^*})E_g}{kT}] \quad \text{Eq. 4-4}$$

$$C_{Auger} = w / n_i^2$$

The Auger coefficient C_{Auger} = 3.74×10^{-30} (cm^6s^{-1}) for room temperature can be obtained. The calculated result implies that the Auger process has a that weak influence on the decay time, it is coincident with the phenomenon we observed

previously.

In contrast to the PL spectrum that indicates several mechanisms of emisssion due to the existence of deep acceptor, shallow acceptor and Urbach tail investigated recently, the reports of carrier recombination dynamics are lack. Thus, we monitored the decay of the PL intensity at different energy of the emission light excited by a 976nm pulse laser. Fig. 4-6(a) shows several time-resolved PL spectra of sample B (carrier concentration~6.4×10^{18} cm^{-3}) monitored at several different energy and 15K. The measured decay times are significant different. The fitted decay times monitored at different photon energies and measured at 15K are plotted in Fig. 4-6(b). with PL spectrum measured at 15K. The lifetime increases with decreasing detection photon energy. This behavior is a characteristic of exciton localization effect, where the decay of excitons should consider the radiative recombination and also the transfer process to the low-energy tail of the localized states. Theoretical analysis [29, 30] of the PL decay time as a function of emission energy was achieved by assuming the density of tail state is the form of $\exp(-E/E_0)$, where E_0 represents the localization depth. The relation between decay time τ and emission energy E is fitted using

$$\tau(E) = \frac{\tau_{rad}}{1+\exp[(E-E_{me})/E_0]} \qquad \text{Eq. 4-5}$$

where τ_{rad} is the radiative lifetime, E_{me} the energy for which the recombination lifetime equals the transfer time. We obtained τ_{rad} ~1.046 ns, E_{me} ~0.765 eV and E_0 ~10 meV. From this result, the degree of localization (E_0) induced by the band tail state is obtained and very close to the activation energy (or the binding energy of shallow acceptors ~ 5-10 meV [11]) which was mentioned earlier.

Fig. 4-7 shows the relation between decay time and emission energy at different temperatures. As the temperature was increased, the decay time at the low energy side decrease significantly and the slope becomes gentle.

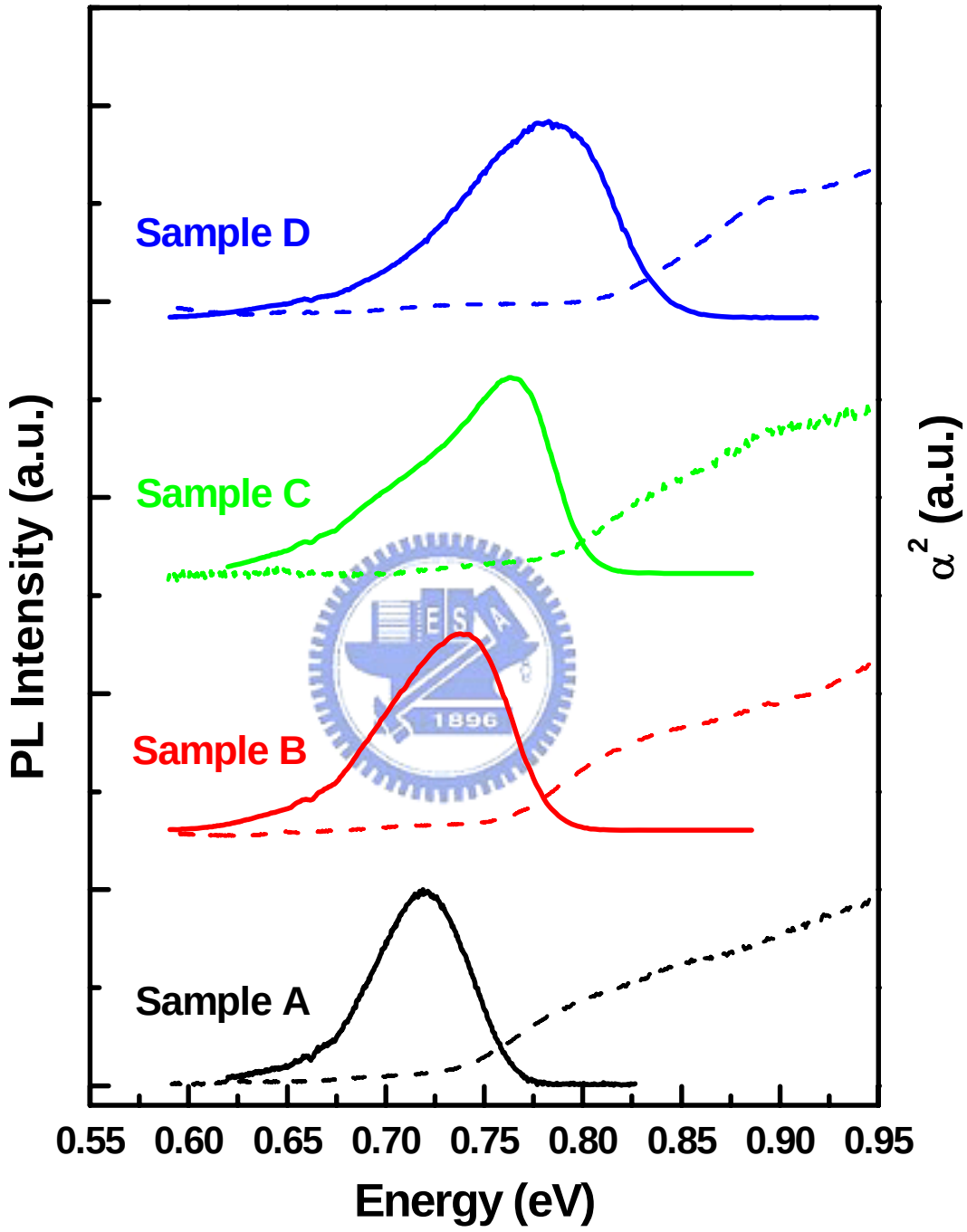

Fig. 4-1 PL (solid lines) and absorption (dashed lines) spectra of InN epilayers measured at low temperature.

(a)

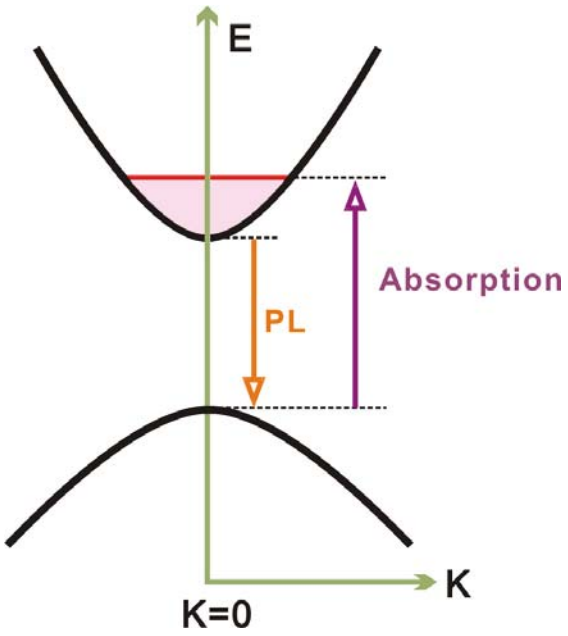

(b)

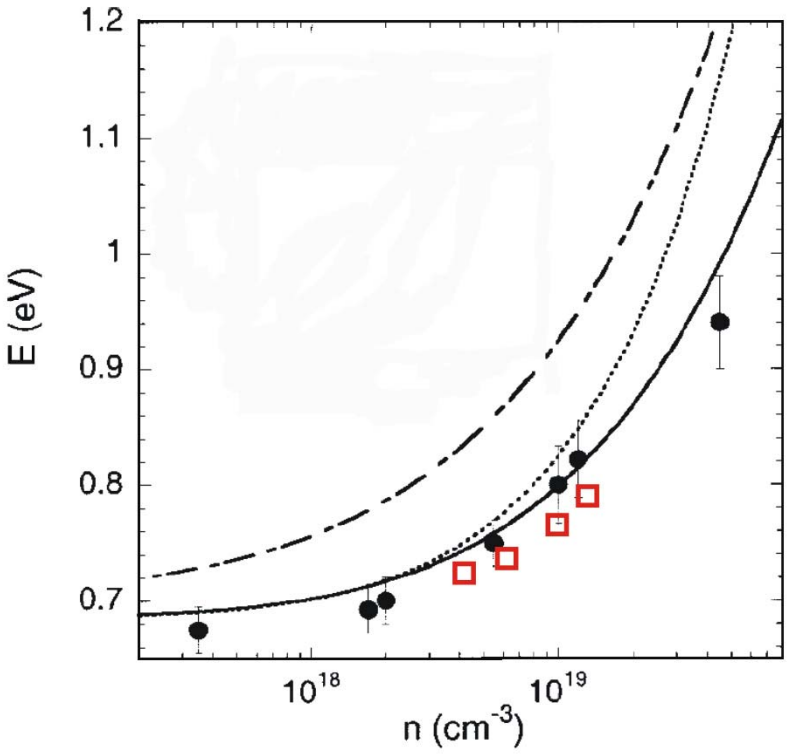

Fig. 4-2 (a) The difference between the absorption process and the PL process in degenerate semiconductors.
(b) The relationship between the absorption edge and the carrier concentration compared with the theoretical calculation given in reference [22]. Open squares are our data points.

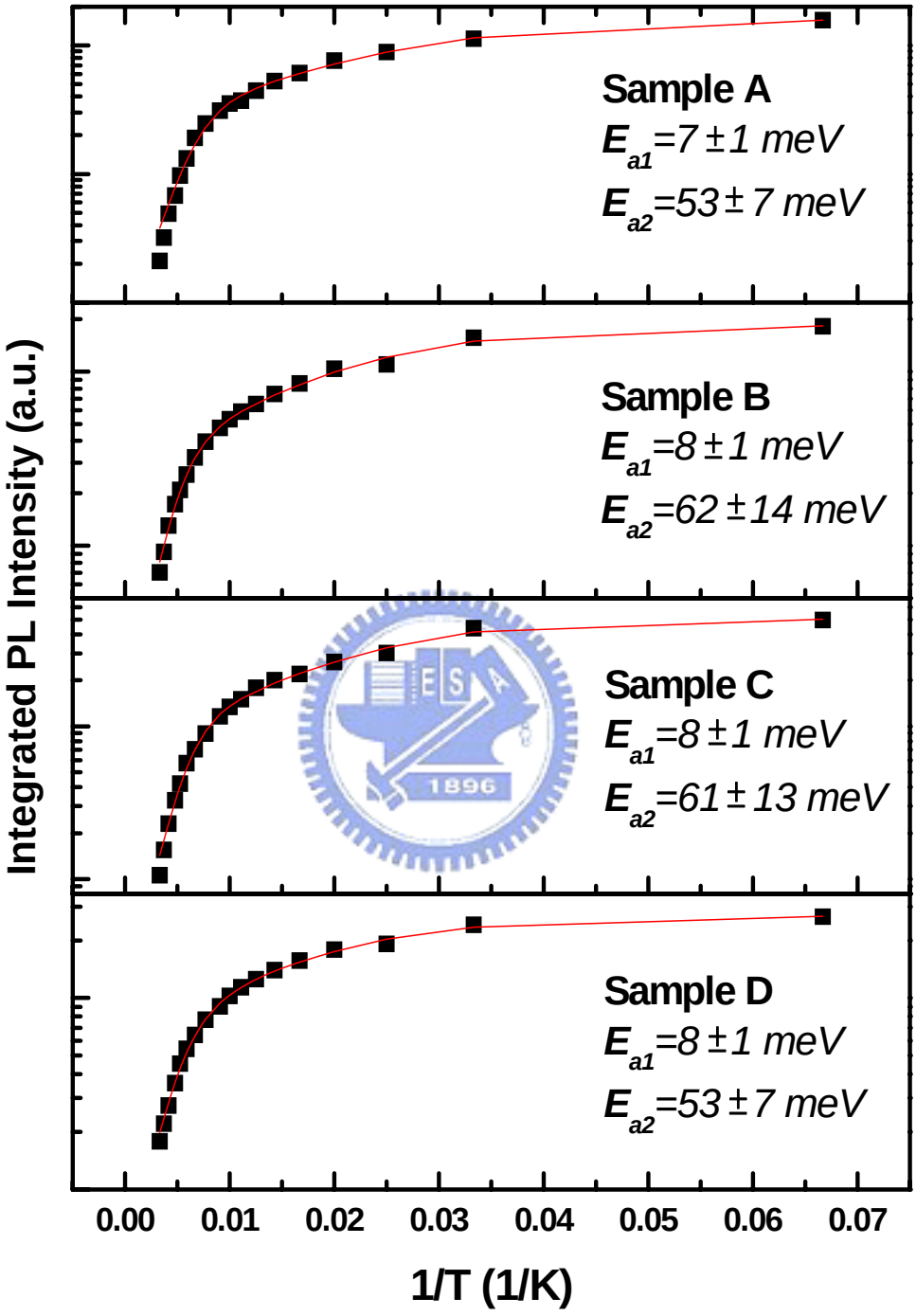

Fig. 4-3 Temperature dependence of the integrated PL intensity of sample A to sample D. E_{a1} and E_{a2} are activation energies obtained by equation 4-1.

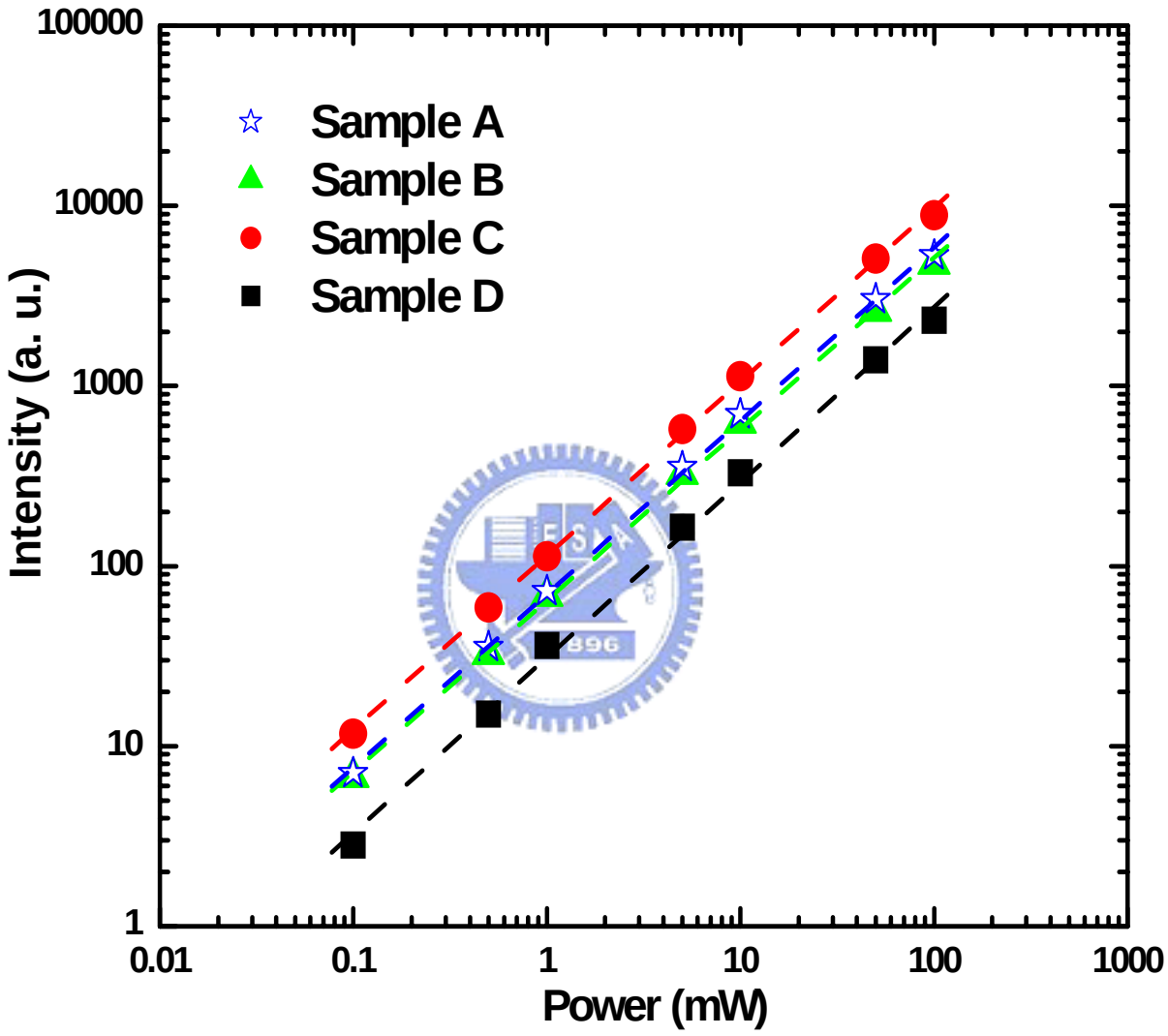

Fig. 4-4 Integrated PL intensity on the logarithmic scale as a function of the excitation power for sample A, B,C and D. Dashed lines are guides to eye.

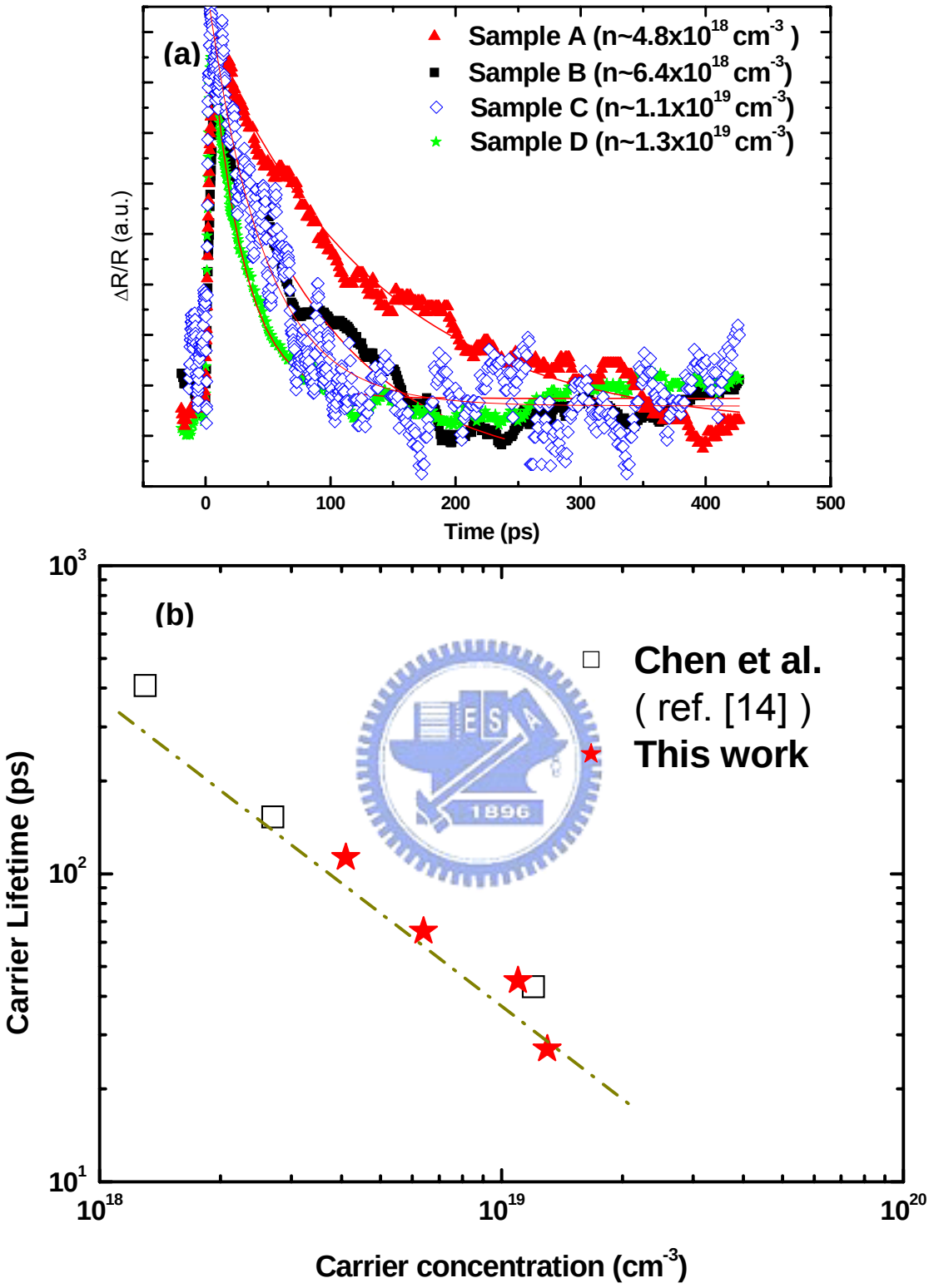

Fig. 4-5 (a) Time resolved differential reflectance signals as a function of time delay excited by a 800nm pulse laser.

(b) Dependence of carrier lifetime on the carrier concentrations.

★ represents our experimental data.

□ are from reference [14].

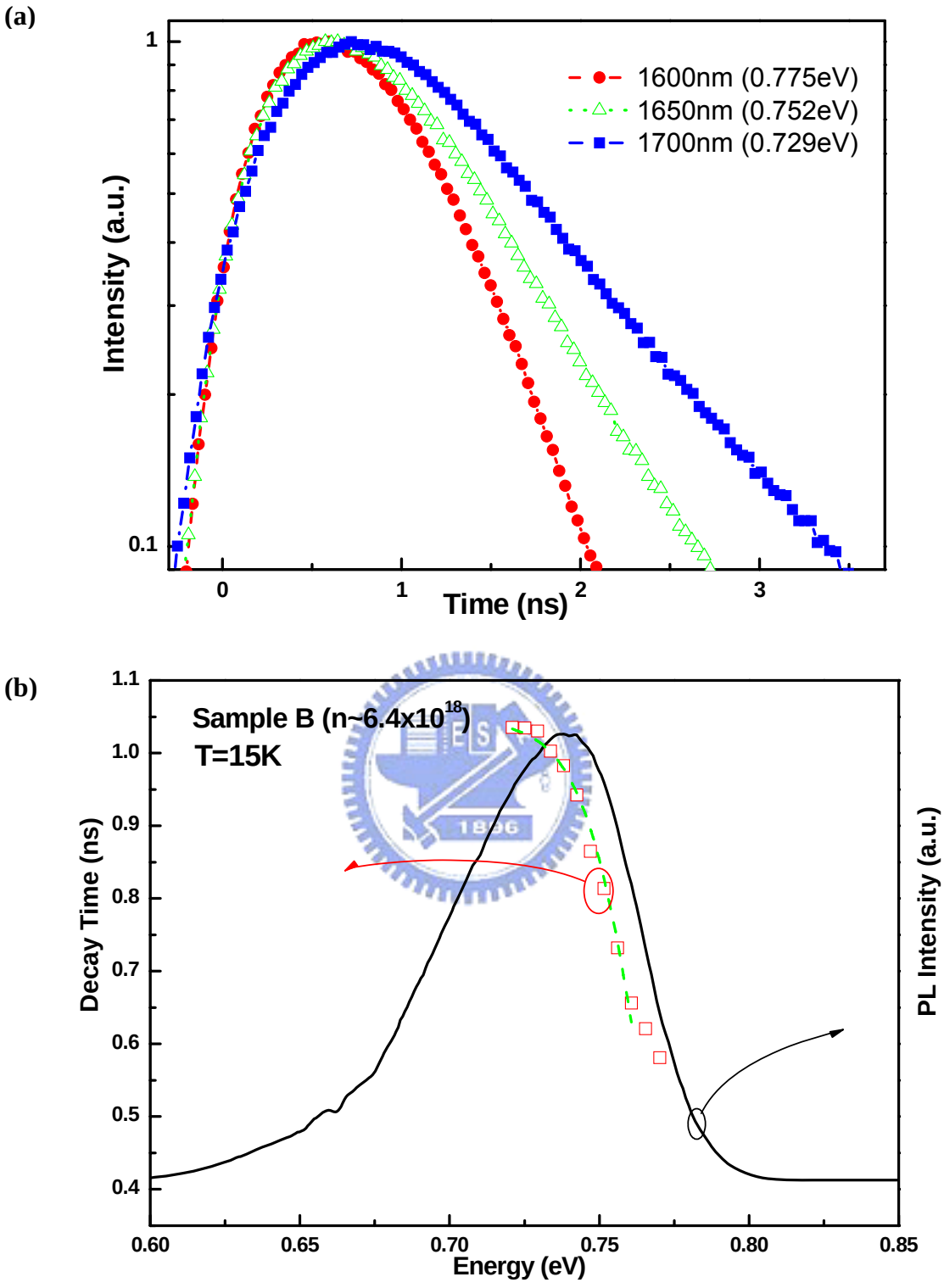

Fig. 4-6 (a) Time-Resolved PL signals of sample B (carrier concentration ~6.4×10^{18} cm^{-3}) measured at 15K.
(b) The fitted decay times monitored at different photon energies are plotted with a PL spectrum measured at 15K.

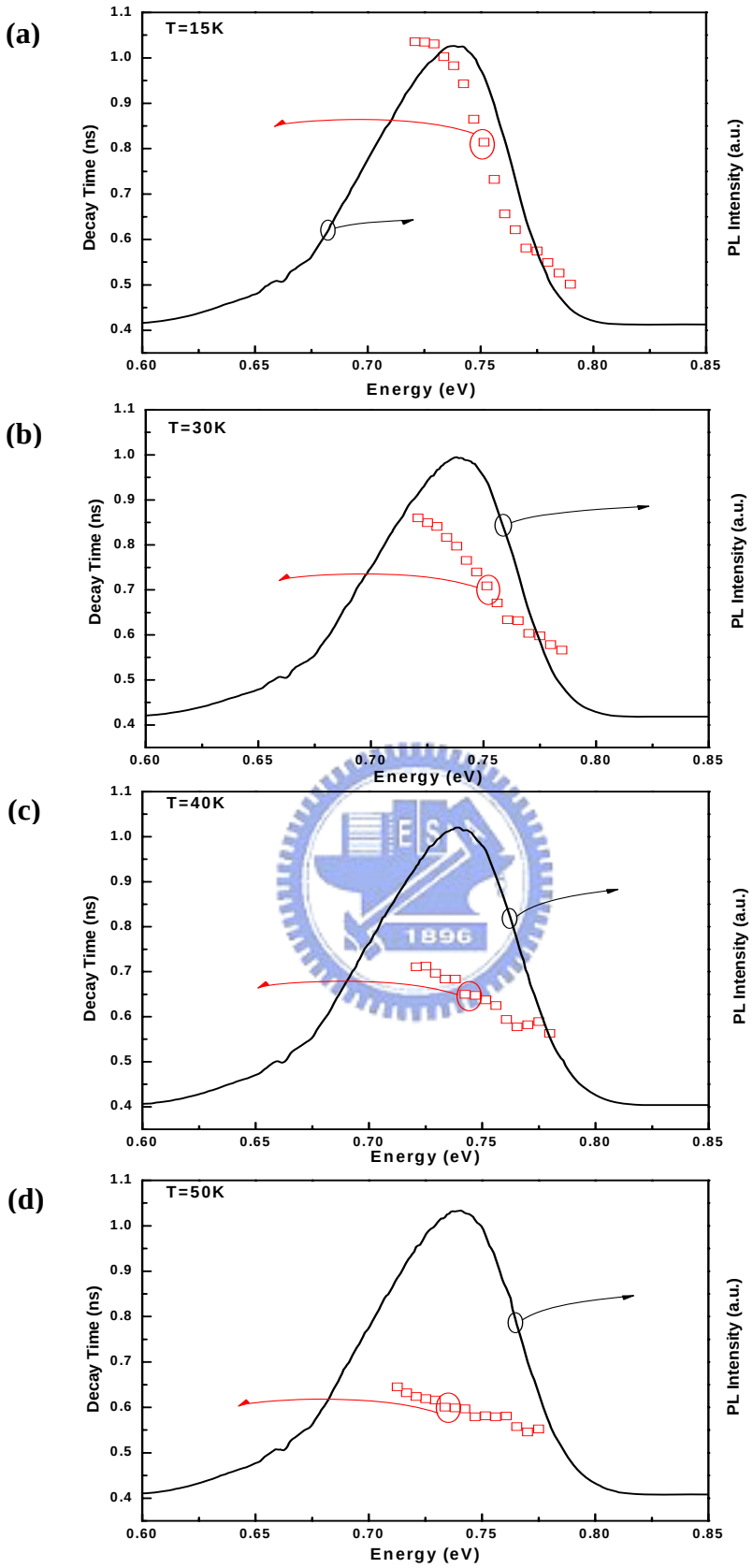

Fig. 4-7 The fitted decay times monitored at different photon energies are plotted with PL spectra for sample B measured at (a) 15K, (b) 30K, (c) 40K and (d) 50K.

Chapter 5 Conclusion

In this study, we investigated the properties of PL and absorption spectra of InN epilayers with carrier concentration from 4.8×10^{18} to 1.3×10^{19} cm^{-3}. Blue shifts of absorption edge and PL peak energy due to the strong Burstein-Moss effect when the carrier concentration increases were observed. Our experimental data are consistent with the theoretical calculation. Typical PL spectra with a highly asymmetric line shape were observed, they indicate the existence of band tail and impurity states. Further, activation energies are obtained from the temperature dependent PL measurements. From the integrated PL intensity versus inverse temperature plot, two activation energies were obtained from the numerical fitting. The smaller one is around 7~10 meV and the larger one is about 50~60 meV. These activation energies correspond to the binding energy of shallow acceptors including Urbach tail and the binding energy of deep acceptors, respectively. The power dependent PL study shows the linear correlation between the integrated PL intensity and the excitation power for all samples, indicating the radiative recombination process dominate at low temperature in our InN epilayer system.

In our study of carrier recombination dynamics, the decay time at room temperature dectreases from 133ps to 27ps when the carrier concentration increases. The carrier lifetime is inversely proportional to carrier concentration (n_0), and reveals the Auger process does not contribute significantly. The carrier lifetime, which includes the transfer time and recombination time, monitored at the emission energy of shallow acceptor is about twice of the lifetime measured at the energy of 10 meV above. The energy is consistent with the localization energy obtained from the fitting of an empirical tail model. When the temperature was increased, the decay time at low

energy side decreased abruptly and the slope became mild. This phenomenon is attributed to the escape of localized carriers.

References

[1] V. Yu. Davydov, A. A. Klochikhin, R. P. Seisyan, V. V. Emtsev, S. V. Ivanov, F. Bechstedt, J. Furthmüller, H. Harima, A. V. Mudryi, J. Aderhold, O. Semchinova, and J. Graul, Phys. Status Solidi B **229**, R1 (2002).

[2] J. Wu, W. Walukiewicz, K. M. Yu, J. W. Ager III, E. E. Haller, H. Lu, W. J. Schaff, Y. Saito, and Y. Nanishi, Appl. Phys. Lett. **80**, 3967 (2002).

[3] T. Matsuoka, H. Okamoto, M. Nakao, H. Harima, and E. Kurimoto, Appl. Phys. Lett. **81**, 1246 (2002).

[4] K. Xu and A. Yoshikawa, Appl. Phys. Lett. **83**, 251 (2003).

[5] S. Gwo, C.-L. Wu, C.-H. Shen, W.-H. Chang, T. M. Hsu, J.-S. Wang, and J.-T. Hsu, Appl. Phys. Lett. **84**, 3765 (2004).

[6] T. L. Tansley and C. P. Foley, J. Appl. Phys. **59**, 3241 (1986).

[7] J. Wu, W. Walukiewicz, K.M. Yu, J.W. Ager III, E. E. Haller, H. Lu, andW. J. Schaff, Appl. Phys. Lett. **80**, 4741 (2002).

[8] http://www.lbl.gov/Science-Articles/Archive/MSD-full-spectrum-solar-cell.html

[9] H. Lu, W. J. Schaff, J. Hwang, H. Wu, W. Yeo, A. Pharkya, and L. F. Eastman, Appl. Phys. Lett. **77**, 2548–550 (2000).

[10] H. Lu, W. J. Schaff, L. F. Eastman, and C. E. Stutz, Appl. Phys. Lett. **82**, 1736 (2003).

[11] A. A. Klochikhin, V. Yu. Davydov, V. V. Emtsev, A. V. Sakharov, V. A. Kapitonov, B. A. Andreev, H. Lu, and W. J. Schaff, Phys. Rev. B **71**, 195207 (2005).

[12] F. Chen, A. N. Cartwright, H. Lu, and W. J. Schaff, Appl. Phys. Lett. **83**, 4984 (2003).

[13] F. Chen, A. N. Cartwright, H. Lu, and W. J. Schaff, Physica E (Amsterdam) **20**, 308 (2004).

[14] F. Chen, A. N. Cartwright, H. Lu, and W. J. Schaff, J. Cryst. Growth **269**, 10 (2004).

[15] F. Chen, A. N. Cartwright, H. Lu, and W. J. Schaff, Phys. Status Solidi A **202**, 768 (2005).

[16] R. Ascazubi, I. Wilke, S. Cho, H. Lu, and W. J. Schaff, Appl. Phys. Lett. **88**, 112111 (2006).

[17] Optical processes in semiconductors, Jacques I. Pankove, Dover Publications, 1975

[18] Semiconductor material and device characterization, Dieter K. Schroder, Wiley-Interscience Publication, 1998

[19] Recombination in semiconductors, Peter T. Landsberg, Cambridge University Press, 1992

[20] Optical properties of solids, Mark Fox, Oxfoed University press, 2001

[21] Introduction to semiconductor physics, Holger T. Grahn., World Scientific, 1999

[22] J. Wu, W. Walukiewicz, W. Shan, K. M. Yu, J. W. Ager III, E. E. Haller, Hai Lu, and William J. Schaff, Phys. Rev. B **66**, 201403 (2002).

[23] Y. H. Wu, K. Arai, and T. Yao, Phys. Rev. B **53**, 10485 (1996).

[24] L.W. Lu, C. L. Yang, J. Wang, I. K. Sou, and W. K. Ge, J. Appl. Phys. **93**, 5325 (2003).

.[25] W. H. Chang, A. T. Chou, W. Y. Chen, H. S. Chang, and T. M. Hsu, Z. Pei, P. S. Chen, S. W. Lee, L. S. Lai, S. C. Lu, and M. J. Tsai, Appl. Phys. Lett. **83**, 2958 (2003).

[26] S.P. Fu , Y.F. Chen, Keewee Tan, Solid State Communications **137**, 203 (2006)

[27] Quantum processes in semiconductors, B. K. Ridley, Oxford University Press, 1993

[28] K. L. Vodopyanov, H. Graener, C. C. Phillips, and T. J. Tate, Phys. Rev. B **46**, 13194-13200 (1992).

[29] C. Gourdon, P. Lavallard, Phys. Status Solidi B **153**, 641 (1989).

[30] S. Sanguinetti, K. Watanabe, T. Tateno, M. Wakaki, N. Koguchi, T. Kuroda, F. Minami, and M. Gurioli, Appl. Phys. Lett. **81**, 613 (2002).